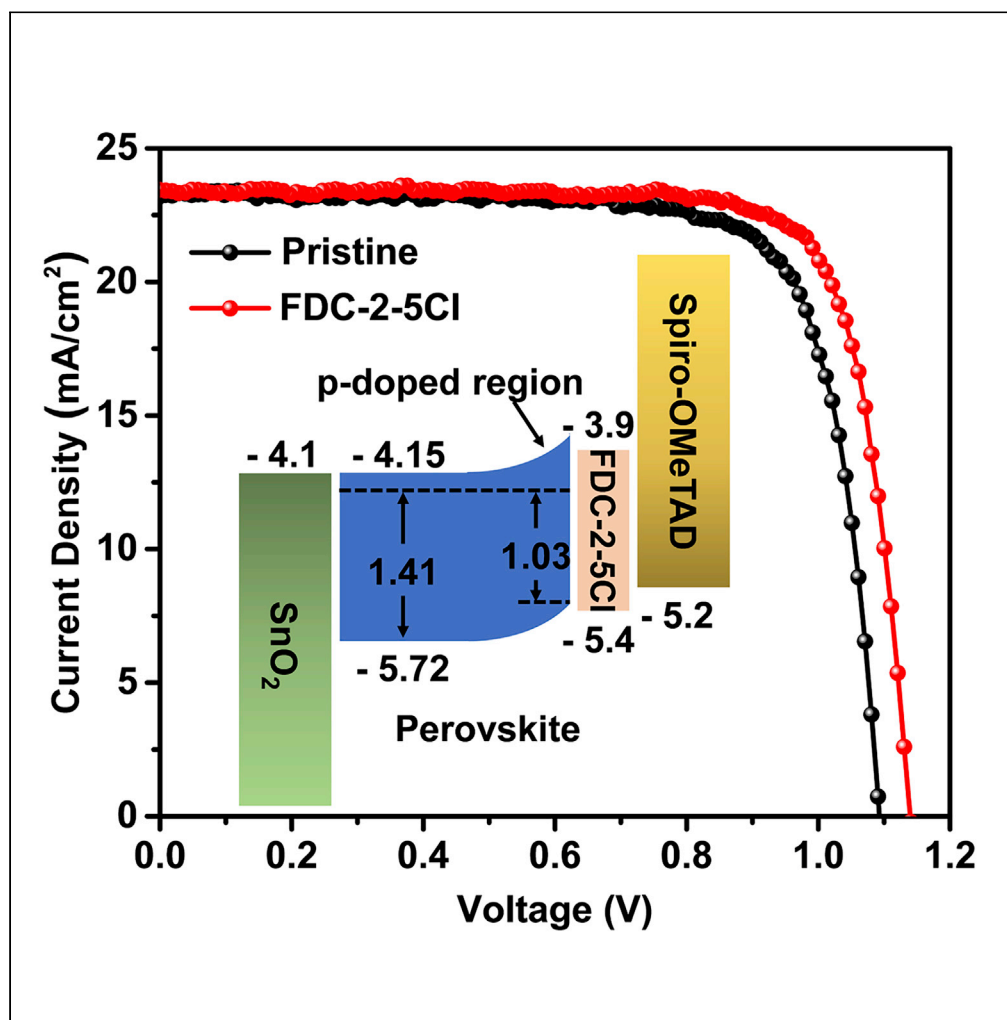**Article**

Synergetic surface charge transfer doping and passivation toward high efficient and stable perovskite solar cells

Xing Guo, Jie Su, Zhenhua Lin, ..., Zebing Zeng, Jingjing Chang, Yue Hao

jjingchang@xidian.edu.cn

HIGHLIGHTS

A benzopentafulvalene compound (FDC-2-5Cl) is used to treat the perovskite film

The FDC-2-5Cl could induce p-type doping and passivation effect on perovskite film

The device with treatment achieves a PCE of 21.16% with a high V_{oc} of 1.14 V

The unencapsulated devices with passivation exhibit outstanding stability

Article

Synergetic surface charge transfer doping and passivation toward high efficient and stable perovskite solar cells

Xing Guo,[1] Jie Su,[1,2] Zhenhua Lin,[1] Xinhao Wang,[3] Qingrui Wang,[1] Zebing Zeng,[3] Jingjing Chang,[1,2,4,*] and Yue Hao[1,2]

SUMMARY

Organic-inorganic lead halide perovskite solar cells (PSCs) have received much attention in the last few years due to the high power conversion efficiency (PCE). Generally, perovskite/charge transport layer interface and the defects at the surface and grain boundaries of perovskite film are important factors for the efficiency and stability of PSCs. Herein, we employ an extended benzopentafulvalenes compound (FDC-2-5Cl) with electron-withdrawing pentachlorophenyl group and favorable energy level as charge transfer molecule to treat the perovskite surface. The FDC-2-5Cl with pentachlorophenyl group could accept the electrons from perovskite as a p-type dopant, and passivate the surface defects. The p-type doping effect of FDC-2-5Cl on perovskite surface induced band bending at perovskite surface, which improves the hole extraction from perovskite. As a result, the PSC with FDC-2-5Cl treatment achieves a PCE of 21.16% with an enhanced open-circuit voltage (V_{oc}) of 1.14 V and outstanding long-term stability.

INTRODUCTION

Owing to the excellent optoelectronic properties, such as strong light absorption (Xiao et al., 2014), long charge carrier lifetime (Stranks et al., 2013), high charge carrier mobility (Wehrenfennig et al., 2014), low exciton binding energy (Lin et al., 2015), and tunable bandgap (Guo et al., 2019; Noh et al., 2013; Zhang et al., 2020), organic-inorganic lead halide perovskite semiconductors have been widely used in solar cells, light-emitting diodes, photodetectors and lasers (Liu et al., 2018; Saidaminov et al., 2015; Seo et al., 2017; Stranks and Snaith, 2015; Zhu et al., 2015). In the last few years, the power conversion efficiency (PCE) of perovskite solar cells (PSCs) has rocked from an initial 3.8% to 25.5%(Kojima et al., 2009; NREL Chart, 2020). However, some core issues limit the commercial application of PSCs. On one hand, due to the solution fabrication process and the ionic nature of perovskite, many defects are formed at the grain boundary and surface of polycrystalline perovskite film, such as halide anion and Pb^{2+} cation vacancies, organic cation vacancies, undercoordinated halide and Pb^{2+} ions, and Pb-I antisite defects (Ball and Petrozza, 2016; Eames et al., 2015; Shao et al., 2014; Sherkar et al., 2017; Shi et al., 2015; Zhou et al., 2019b). These non-negligible defects at grain boundary and interface can act as recombination centers and cause serious charge carrier recombination, which is one of the main barriers for the improvement of PSC device performance (Li et al., 2019; Qian et al., 2019). Except efficiency, the relatively poor device stability is another serious issue for PSCs. Researches show that defects are involved in the decomposition process of perovskite films, leading to the long-term instability of PSCs (Aristidou et al., 2017; Berhe et al., 2016; Saidaminov et al., 2018; Wang et al., 2016).

It's crucial to suppress the defects at grain boundary and surface of perovskite for improving the efficiency and stability of PSCs. Various passivation agents, such as metal halides, fullerenes and their derivatives, polymers, and organic halide salts have been used to passivate the defects of perovskite film (Meng et al., 2018; Son et al., 2018; Turren-Cruz et al., 2018; Yang et al., 2018; Zhao et al., 2018). Among them, organic molecules exhibit great potential due to their diversity of structural functionality for performance improvement and hydrophobicity enhancement to protect perovskites against moisture and oxygen. For example, Tavakoli et al. introduced 1-adamantylamine hydrochloride (ADAHCl) with 1-adamantylamine functional group to passivate surface defects of perovskite. The device with formamidinium chloride (FACl) and ADAHCl passivation achieved a higher PCE of 21.2% compared to that with FACl (20.52%)

[1]State Key Discipline Laboratory of Wide Band Gap Semiconductor Tecchnology, Shaanxi Joint Key Laboratory of Graphene, School of Microelectronics, Xidian University, 2 South Taibai Road, Xi'an 710071, China

[2]Advanced Interdisciplinary Research Center for Flexible Electronics, Xidian University, 2 South Taibai Road, Xi'an 710071, China

[3]State Key Laboratory of Chemo/Biosensing and Chemometrics, Hunan University, Changsha 410082, P. R. China

[4]Lead contact

*Correspondence: jjingchang@xidian.edu.cn

https://doi.org/10.1016/j.isci.2021.102276

and reference (19.43%) (Tavakoli et al., 2019). However, most of surface passivation methods for perovskite film only focus on the surface defects, and the mismatch of energy band between perovskite and 2,2′,7,7′-tetrakis[N,N-di(4-methoxyphenyl)amino]-9,9′-spirobifluorene (spiro-OMeTAD) is often overlooked, which influences the charge transfer at perovskite/spiro-OMeTAD interface (Guo et al., 2018b; Zhou et al., 2019a). Hence, the organic molecule passivator with suitable energy level and charge transfer capability is beneficial for improved charge transfer at the perovskite/Spiro-OMeTAD interface.

Meanwhile, similar with graphene, it is thought that the organic molecules donor or acceptor could induce charge transfer doping on the organic or inorganic surface due to strong molecular interaction, which can adjust the surface properties of perovskite film further. For example, Noel et al. introduced the molybdenum tris(1-(trifluoroethanoyl)-2-(trifluoromethyl)ethane-1,2-dithiolene) (Mo(tfd-COCF$_3$)$_3$) as molecular doping on perovskite surface, they found that the dopant-treated perovskite interface become more p-type due to the charge transfer from perovskite to Mo(tfd-COCF$_3$)$_3$. By using the molecular p-doping, they discarded the 4-tert butylpyridine (tBP) and achieved a PSC with improved thermal stability(Noel et al., 2019). Jiang et al. observed the p-type doping behavior on 4,4′,4″,4‴-(pyrazine-2,3,5,6-tetrayl) tetrakis (N,Nbis(4-methoxyphenyl) aniline) PT-TPA treated perovskite surface, the p-type doping forms the bending of perovskite band, which improve the hole transfer from perovskite to hole transport layer (HTL) (Jiang et al., 2020).

In this study, we report an extended benzopentafulvalenes compound (FDC-2-5Cl) with favorable energy level for surface treatment of perovskite film. The electron-withdrawing chlorine group in FDC-2-5Cl could passivate the undercoordinated Pb^{2+}, and the FDC-2-5Cl could also form hydrogen-bond with halide anions in perovskite, which could passivate the undercoordinated iodine. Meanwhile, the electron-withdrawing pentachlorophenyl group could accept electrons from perovskite and induce p-doping of perovskite surface. The p-doping of perovskite surface causes the band bending and improves the energy band alignment at perovskite/HTL interface, which promotes the hole extraction and reduces the electron-hole recombination at perovskite/HTL interface. Further first-principles calculations reveal that the FDC-2-5Cl treatment could induce charge transfer doping, increase the defect formation energy and reduce the surface energy of perovskite. After being passivated with FDC-2-5Cl, the PSC reached a high PCE of 21.16% (20.7% of stabilized efficiency) with a high open circuit voltage (V_{oc}) of 1.14 V. Meanwhile, the FDC-2-5Cl treatment also improved the stability of PSCs, with 88% of its initial PCE after 1008 hr storage in air.

RESULTS AND DISCUSSION

Influence of FDC-2-5Cl on perovskite thin films

We used a two-step process to fabricate the Cs$_{0.05}$MA$_{0.95-x}$FA$_x$PbI$_{3-y}$Cl$_y$ (y < 0.03) perovskite film. The FDC-2-5Cl passivation layer was introduced by solution coating the FDC-2-5Cl solution in chlorobenzene on perovskite film and annealing at 100°C for 3 min. The PSC structure is shown in Figure 1A, and the inset shows the molecular structure of FDC-2-5Cl compound which contains two pentachlorophenyl groups and the aromatic nucleus structure. The crystal structure and crystal packing of FDC-2-5Cl are shown in Figures 1B and S1 in supplemental information. From the crystal packing, the FDC-2-5Cl has dense π-π and halogen-π interactions, which is crucial for carrier transport (Wang et al., 2020). The energy levels and electrical characteristics of FDC-2-5Cl are listed in Figure S2 and Table S1 in supplemental information.

To confirm the existence of FDC-2-5Cl on perovskite surface and the bonding state of FDC-2-5Cl with perovskite film, we carried out the X-ray photoelectron spectroscopy (XPS) measurement. Figure S3 shows the full XPS spectra of perovskite film without and with FDC-2-5Cl treatment, and the significant change of Cl 2p indicates the existence of FDC-2-5Cl on perovskite film. Figures 1C–1F show the high-resolution C 1s, Cl 2p, Pb 4f, and I 3d XPS spectra, respectively. For the pristine perovskite film, the C 1s peak could be divided to three peaks located at 284.07 eV, 285.27 eV, and 287.27 eV, corresponding to the C-C peak, C-N peak and C=O peak, respectively. For the perovskite film with FDC-2-5Cl treatment, the peaks located at 283.67 eV and 285.57 eV are also corresponding to the C-C peak and C-N peak, respectively. Noticeably, the C=O peak at 287.17 eV is significantly suppressed in perovskite film with FDC-2-5Cl treatment, and the formation of C=O bond is related to the reaction between the organic cations in perovskite and absorbed oxygen and moisture when exposing to ambient air (Chen et al., 2018; Lv et al., 2018; Sun et al., 2017). This result indicates that the FDC-2-5Cl treatment could enhance the tolerance of perovskite film to oxygen and moisture. We also observed a new peak at 289.87 eV for perovskite film with FDC-2-5Cl treatment, corresponding to the π-π interaction between the FDC-2-5Cl molecules (Jiang et al., 2019; Li et al., 2020). From
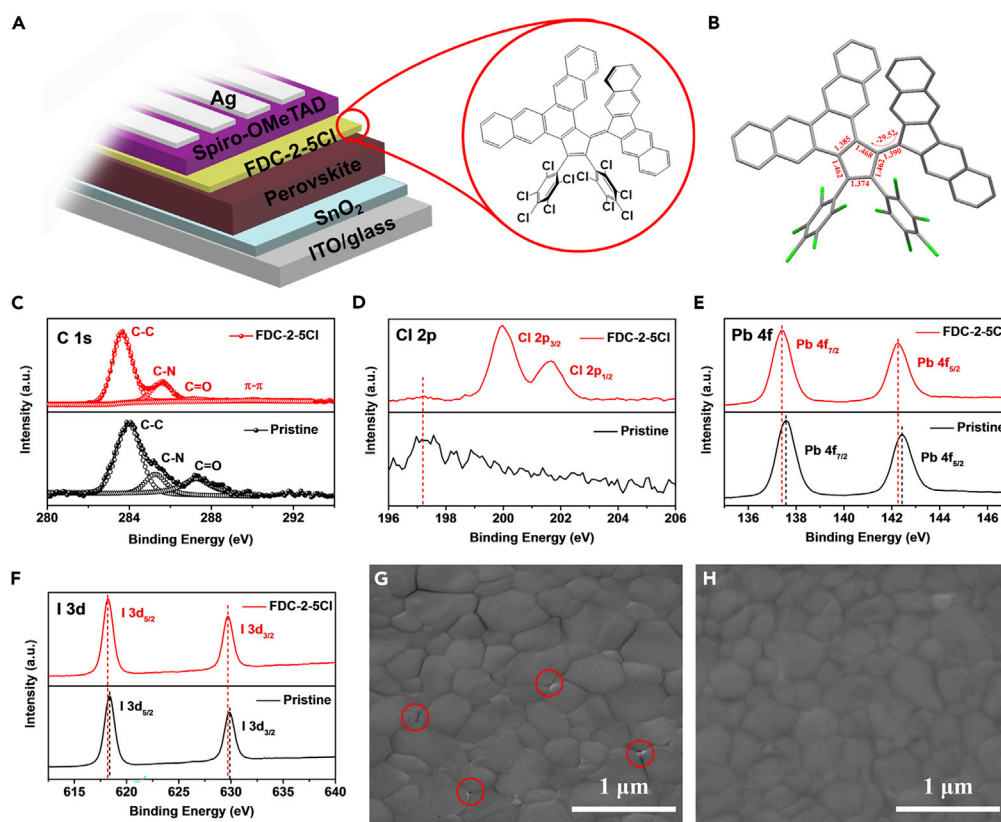
Figure 1. The device structure and XPS results of perovskite films

(A) The device structure of PSCs, the inset is the molecular structure of FDC-2-5Cl.

(B) Crystal structure of FDC-2-5Cl.

(C–F) High-resolution XPS spectra of (C) C 1s, (D) Cl 2p, (E) Pb 4f, and (F) I 3d.

(G and H) Top-view SEM images of perovskite films (G) without and (H) with FDC-2-5Cl treatment.

Figure 1D, the peaks located at 197.20 eV for the pristine and FDC-2-5Cl treated perovskite films are corresponding to the Cl of perovskite film. While for the FDC-2-5Cl treated perovskite film, the new peaks located at 199.97 eV and 201.67 eV could be observed, corresponding to the Cl in FDC-2-5Cl. From Figures 1E and 1F, after being treated by FDC-2-5Cl, the Pb $4f_{7/2}$ and Pb $4f_{5/2}$ peaks located at 137.58 eV and 142.42 eV shift to lower binding energies of 137.40 eV and 142.27 eV, and the I $3d_{5/2}$ and I $3d_{3/2}$ located at 618.36 eV and 629.86 eV shift to lower binding energies of 618.19 eV and 629.69 eV, respectively. The down shift of Pb and I peaks indicates a shift of Femi level of perovskite, which indicates the p-doping of perovskite surface (Jiang et al., 2020; Noel et al., 2019).

The scanning electron microscope (SEM) measurement was carried out to study the surface morphology of perovskite film without and with FDC-2-5Cl treatment. As shown in Figures 1G and 1H, all the perovskite films show uniform and smooth surface morphology. However, the pristine perovskite film shows significant pinholes and grain boundary. As reported, many defects lie at grain boundary and cause serious charge recombination. While for the perovskite film with FDC-2-5Cl treatment, the grain boundary becomes blurry, which indicates the FDC-2-5Cl treatment is help to passivate the grain boundary. We also measured the energy dispersive spectroscopy of perovskite films without and with FDC-2-5Cl treatment, as shown in Figure S4. All elements in the perovskite films without and with FDC-2-5Cl treatment are uniformly distributed, but the atomic ratio of Cl increases after FDC-2-5Cl treatment due to the abundant chlorine group in FDC-2-5Cl molecule. We further studied the influence of FDC-2-5Cl treatment on the crystallinity of perovskite film. Figure S5 shows the X-ray diffraction (XRD) patterns of perovskite films without and with FDC-2-5Cl treatment. All the patterns show significant diffraction peak at 14.01°, 28.37°, and 31.68°, corresponding to the (110), (220), and (310) crystal planes, respectively (Guo et al., 2018a). The FDC-2-5Cl treatment does not introduce any new peaks in the XRD spectrum of perovskite film, which means the similar
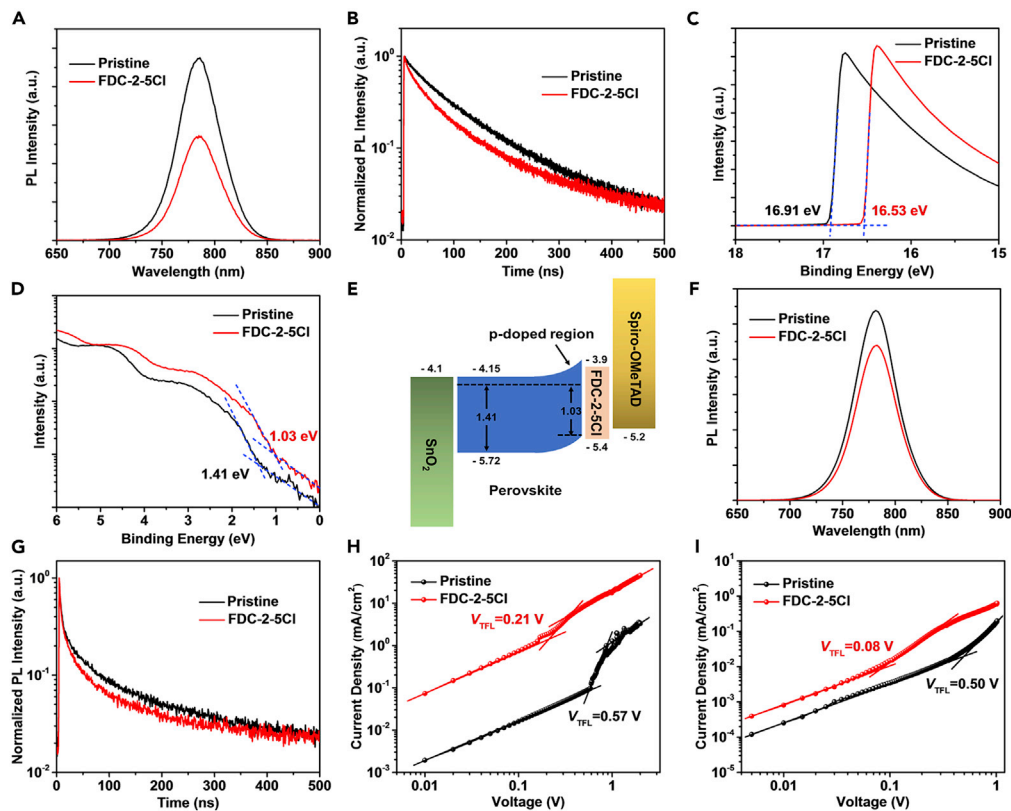
Figure 2. Characterizations of carrier lifetime, charge transfer, and trap density of perovskite film

(A and B) (A) PL and (B) TR-PL spectra of perovskite films without and with FDC-2-5Cl treatment. UPS spectra of perovskite films with and without FDC-2-5Cl treatment.

(C and D) (C) The secondary electron cutoff region and (D) the frontier electronic structure region.

(E) Illustration of proposed energy band bending at the surface of the perovskite due to the charge transfer from perovskite to FDC-2-5Cl.

(F and G) (F) PL and (G) TR-PL spectra of perovskite/spiro-OMeTAD films without and with FDC-2-5Cl treatment.

(H and I) The dark *J-V* characteristics of devices with structure of (H) glass/ITO/SnO$_2$/perovskite/PCBM/Ag and (I) glass/ITO/NiO/perovskite/spiro-OMeTAD/Ag.

crystal structure of perovskite film after FDC-2-5Cl treatment. Meanwhile, the peak intensity of perovskite film slightly increases after being passivated by FDC-2-5Cl, mainly because the surface treatment of FDC-2-5Cl with a low concentration and short annealing time is hard to influence the perovskite film crystal significantly. Figure S6 shows the UV-vis absorption spectra of perovskite films with and without FDC-2-5Cl treatment. The perovskite film with FDC-2-5Cl treatment shows similar absorption compared to pristine perovskite film, which is consistent with the XRD result.

The influence of FDC-2-5Cl treatment on photogenerated carrier dynamics of perovskite film was studied by the steady-state photoluminescence (PL) spectra in Figure 2A. The PL intensity of perovskite film with FDC-2-5Cl treatment is obviously quenched compared to that of pristine perovskite film mainly due to charge transfer induced quenching effect (Biswas et al., 2020; Muduli et al., 2018). Research studies show that the passivation could reduce the non-radiative recombination caused by defects, and the PL intensity would increase after passivation, which is in contrast with the PL result in Figure 2A. Here the PL intensity change should be mainly caused by the effect of charge transfer induced quenching. Further, we carried out time-resolved photoluminescence (TR-PL) measurements to study the photogenerated carrier lifetime, as shown in Figure 2B. Table S2 lists the fitting parameters of TR-PL curves fitted by a biexponential function. The perovskite film with FDC-2-5Cl treatment exhibits a shorter average lifetime of 73.52 ns compared with pristine perovskite film (94.60 ns), which indicates the existence of charge transfer from perovskite to FDC-2-5Cl.

To further clarify the cause of charge transfer, the ultraviolet photoelectron spectroscopy (UPS) of perovskite without and with FDC-2-5Cl treatment were measured. As shown in Figures 2C and 2D. The work function (W_F) is determined form the secondary electron cutoff region in Figure 2C, where the W_F of perovskite film significantly increased from 4.31 to 4.69 eV after FDC-2-5Cl treatment. The frontier electronic structure region is displayed as logarithmic coordinates to confirm the valence band maximum (VBM) refered to Fermi level (E_F) in Figure 2D. The Energy level schemes of perovskite film without and with FDC-2-5Cl treatment is shown in Figure S7, the optical bandgap of perovskite film (1.57 eV) could be calculated from the UV-vis spectra. The E_F of perovskite is much closer to VBM after FDC-2-5Cl treatment, which indicates the FDC-2-5Cl caused a p-type doping to perovskite surface. This result is consistent with the down shift of Pb and I XPS peak. The p-type doping would drive the band bending at perovskite surface, as shown in Figure 2E. The band bending improve the hole extraction at perovskite/HTL interface, which caused the quenching of PL and decreased carrier lifetime.

We also studied the influence of FDC-2-5Cl treatment on the charger transfer at perovskite/spiro-OMeTAD interface. The PL and TR-PL spectra of perovskite/spiro-OMeTAD films without and with FDC-2-5Cl treatment were measured and shown in Figures 2F and 2G. The PL spectrum of perovskite/spiro-OMeTAD film with FDC-2-5Cl treatment shows a significant quenching compared to that of perovskite/spiro-OMeTAD film, indicating an increased charger transfer from perovskite film to spiro-OMeTAD HTL. The carrier lifetimes of perovskite/spiro-OMeTAD film without and with FDC-2-5Cl treatment were also calculated by fitting the TR-PL curves with a biexponential decay model and the fitting times are listed in Table S2. The carrier lifetime of perovskite/spiro-OMeTAD with FDC-2-5Cl treatment is 9.92 ns, shorter than that of pristine perovskite/spiro-OMeTAD film. The decreased carrier lifetime means the improved charge transfer at perovskite/spiro-OMeTAD interface. This result is not only because FDC-2-5Cl passivates the defects at perovskite/spiro-OMeTAD interface and reduces the non-radiative recombination caused by defects but also due to band bending of perovskite caused by the p-type doping of FDC-2-5Cl. Meanwhile, the HOMO energy level of FDC-2-5Cl (−5.45 eV) is between the VBM of perovskite film and the HOMO of spiro-OMeTAD, and the FDC-2-5Cl shows a high hole mobility closed to spiro-OMeTAD which improves the energy band alignment of perovskite/spiro-OMeTAD interface and enhances the charge transfer.

To further evaluate the influence of FDC-2-5Cl treatment on trap density in perovskite film, we carried out the space charge-limited-current (SCLC) measurement. The electron-only device and hole-only device with the structure of glass/ITO/SnO$_2$/perovskite/PCBM/Ag and glass/ITO/NiO/perovskite/spiro-OMeTAD/Ag were fabricated for SCLC measurement, respectively. Figures 2H and 2I show the dark current density-voltage (J-V) curves of devices without and with FDC-2-5Cl treatment. At low bias region, the current and voltage show a linear relationship. When the voltage increases, the trap states are filled, the current increases dramatically, and the corresponding voltage is called trap-filled limit voltage (V_{TFL}). The trap density (N_{trap}) can be calculated from the equation $N_{trap}=(2\varepsilon\varepsilon_0 V_{TFL})/(eL^2)$, where L is the thickness of perovskite film (~500 nm, measured by step profiler), e is the elementary charge, ε is relative dielectric constant, and ε_0 is vacuum permittivity. For the electron-only device, the V_{TFL} are 0.57 V and 0.21 V for perovskite films without and with FDC-2-5Cl treatment, respectively. The calculated N_{trap} are 1.64×10^{15} cm^{-3} and 6.04×10^{14} cm^{-3} for perovskite films without and with FDC-2-5Cl treatment. Similarly, for the hole-only device, the V_{TFL} are 0.50 V and 0.08 V for perovskite films without and with FDC-2-5Cl treatment, and the N_{trap} are calculated to 1.44×10^{15} cm^{-3} and 2.30×10^{14} cm^{-3} for perovskite films without and with FDC-2-5Cl treatment, respectively. All the perovskite films with FDC-2-5Cl treatment show the decreased trap density, which indicates that the FDC-2-5Cl treatment could effectively passivate defects at perovskite surface.

DFT calculation results

First-principles calculations were performed to explore the micro-structure and electronic properties of perovskite surface treated by FDC-2-5Cl. Previous studies have pointed that vacancies and antisite defects are formed at the surface of perovskite film unavoidably (Zou et al., 2019). Thus, the antisite defect I_{Pb} at the PbI-terminated MAPbI$_3$ (001) surface and I-vacancy (V_I) at the MAI-terminated MAPbI$_3$ (001) surface are considered. Since the FDC-2-5Cl possesses a large number of atoms, the MAPbI$_3$ surface absorbed FDC-2-5Cl (MAPbI$_3$@FDC-2-5Cl) complete model is too big to beyond the limitation of DFT. The MAPbI$_3$@FDC-2-5Cl is simplified and demonstrated in Figures 3 and S8 (the detailed models and calculation details are given in the supplemental information). Similar simplifications have been successfully used in the perovskite surface absorbed with other large molecular (Wolff et al., 2020; Yue et al., 2019). From Figure 3A, an evidently structural disorder is observed for the MAI-terminated MAPbI$_3$ (001) surface with V_I. After absorbing FDC-2-5Cl, such disorder is eased since the
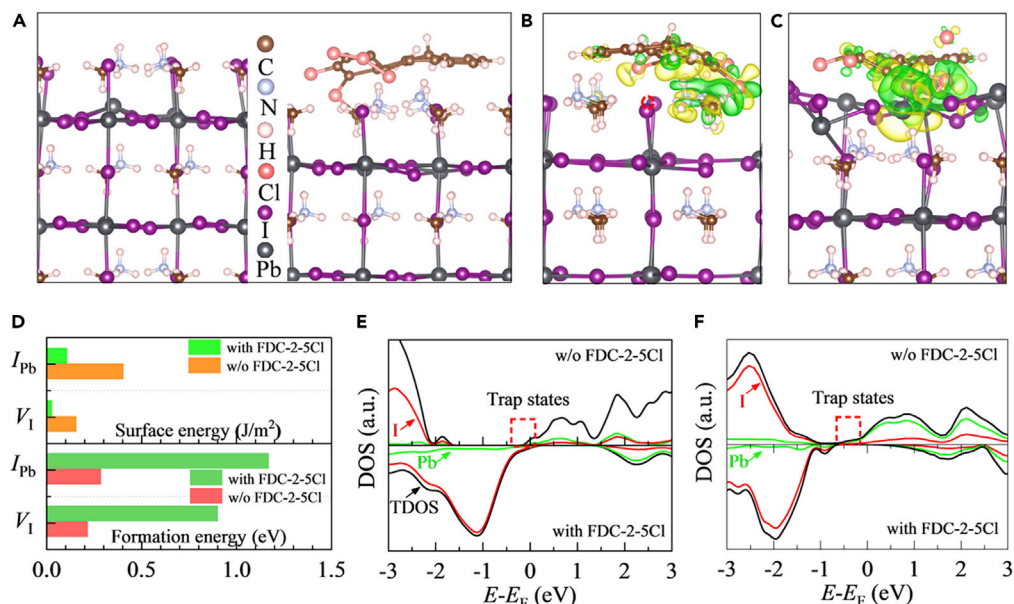
Figure 3. First-principle calculations

(A–C) (A) Side views of FDC-2-5Cl (left) unpassivated and (right) passivated perovskite surfaces with V_I. Charge density difference of FDC-2-5Cl passivated perovskite surface with (B) V_I and (C) I_{Pb}. The green and yellow regions represent the electron depletion and accumulation, respectively.

(D) Surface energy and defect formation energy of perovskite surface with V_I and I_{Pb} tuned by FDC-2-5Cl treatment.

(E and F) Density of states of FDC-2-5Cl passivated and unpassivated perovskite surfaces with (E) V_I and (F) I_{Pb}.

FDC-2-5Cl treatment draws electrons from the perovskite surface so that the Pb-I bonds at the perovskite surface are shrinked and close to those in the bulk perovskite, as seen in Figures 3A and 3B. Thus, the enhanced peak intensity of perovskite film with FDC-2-5Cl treatment is measured by XRD. In addition, the charge transfer is mainly located between Cl atoms of FDC-2-5Cl and Pb ions around V_I and MA cations of perovskite surface, suggesting the formation of Pb-Cl and MA-Cl bonds between defective perovskite surface and FDC-2-5Cl. These bonds occupy the V_I and limit the surface ion migration, so the defect formation energy and surface energy are enlarged and reduced, respectively, as listed in Figure 3D. It means that the the FDC-2-5Cl impedes the surface V_I formation and enhances the stability of perovskite surface. In addition, it can be seen from Figure 3E that the impurity levels induced by the surface V_I which are served as the nonradiative recombination center and prejudice the efficiency of PSC, can be eliminated by the FDC-2-5Cl due to additional charge transfer between FDC-2-5Cl and surface defects. This result confirms the p-type doping effect of FDC-2-5Cl to perovskite surface. Compared to the FDC-2-5Cl passivated surface V_I, similar characters are observed for the FDC-2-5Cl passivated surface antisite defect I_{Pb}. Moreover, additional chemical bonds between the H atom of FDC-2-5Cl and the I ion of perovskite surface are formed, as demonstrated in Figure 3C. Thus, the corresponding defect formation energy and surface energy are improved and reduced, respectively, and the impurity levels induced by I_{Pb} are vanished by FDC-2-5Cl treatment (see Figures 3D and 3F). Thus, both the structural and optoelectronic properties of FDC-2-5Cl passivated perovskite film are improved in experiment.

Device performance of PSCs

We further evaluated the influence of FDC-2-5Cl treatment on PSCs performance based on the device shown in Figure 1A. We first optimized the concentration of FDC-2-5Cl, and the results are shown in Figure S9. The optimal concentration of FDC-2-5Cl is 1.0 mg/mL. Figure 4A shows the energy band structure of all materials in PSCs which has been reported in our previous works(Wang et al., 2020; Guo et al., 2018a). The HOMO of FDC-2-5Cl (−5.45 eV) is between the valence band of the perovskite and the HOMO of spiro-OMeTAD and shows a good energy band alignment with perovskite and spiro-OMeTAD. The p-type doping of FDC-2-5Cl caused the band bending at perovskite surface, the VBM of perovskite is closer to the HOMO of sprio-OMeTAD. The hole mobility of FDC-2-5Cl is 1.06×10^{-4} cm^{2}V^{-1}s^{-1}, which is close to that of spiro-OMeTAD (1.1×10^{-3} cm^{2}V^{-1}s^{-1}) (Xi et al., 2017). The good energy band alignment and high hole mobility of FDC-2-5Cl could help to enhance the charge transfer at perovskite/spiro-OMeTAD
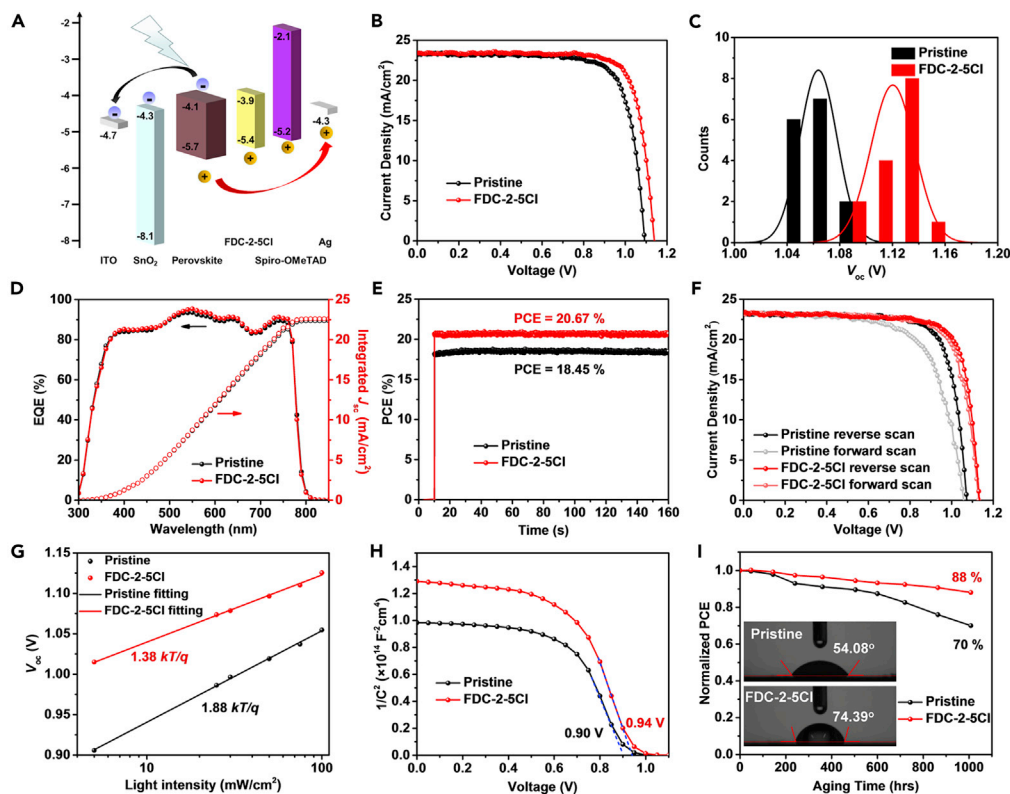
Figure 4. Photovoltaic characteristics of PSCs without and with treatment

(A) The energy band structure of PSCs.

(B) *J-V* curves of PSCs without and with FDC-2-5Cl treatment.

(C) V_{oc} distribution of PSCs without and with FDC-2-5Cl treatment.

(D) EQE spectra of the PSC without and with FDC-2-5Cl treatment.

(E and F) Steady state outputs of PCE (E) and *J - V* hysteresis (F) of the best PSCs without and with FDC-2-5Cl treatment.

(G and H) V_{oc} as a function of light intensity (G), and *C - V* curves spectra (H) of PSCs without and with FDC-2-5Cl treatment.

(I) Long-term stability of PSCs without and with FDC-2-5Cl treatment. (inset) Water contact angles of perovskite films without and with FDC-2-5Cl treatment.

interface. The *J - V* characteristics of champion devices without and with FDC-2-5Cl treatment are shown in Figure 4B. The pristine device shows a PCE 19.53% with a short-circuit current density (J_{sc}) of 23.25 mA/cm^2, a V_{oc} of 1.09 V, and a fill factor (FF) of 0.77. The device with FDC-2-5Cl treatment exhibits an improved PCE of 21.16% with a J_{sc} of 23.41 mA/cm^2, a V_{oc} of 1.14 V, and an FF of 0.79. The improved PCE of PSCs with FDC-2-5Cl treatment is mainly attributed to the significantly improved V_{oc}. We also counted the V_{oc} of PSCs without and with FDC-2-5Cl treatment, as shown in Figure 4C. The result also indicates a significant improved V_{oc}, which is due to the enhanced hole extraction and decreased defects density at perovskite/ HTL interface after FDC-2-5Cl treatment. The statistical results of other photovoltaic parameters based on 15 cells are shown in Figure S10. The PSC with FDC-2-5Cl treatment also shows a slightly improved J_{sc}. We further verified the J_{sc} of *J-V* measurement by the external quantum efficiency (EQE) measurement in Figure 4D. The integrated current densities from EQE measurement are 22.36 mA/cm^2 and 22.60 mA/cm^2 for perovskite films without and with FDC-2-5Cl treatment, respectively. This result is in good agreement with the improvement of J_{sc} from *J - V* measurement. Figure 4E exhibits the stay-state output of devices. The PSC with FDC-2-5Cl treatment shows a higher steady output PCE of 20.67% than that of 18.45% for pristine PSC. However, the device with FDC-2-5Cl treatment shows a negligible saturated time compared to pristine devices, and the saturated time is considered to be related to defects filling, which indicates that FDC-2-5Cl treatment effectively suppresses the defects at surface of perovskite film. The dark *J-V* characteristics of PSCs without and with FDC-2-5Cl treatment are shown in Figure S11. The PSC with FDC-2-5Cl shows lower dark current than the pristine PSC, the dark current is considered to be related to the trap states in the bulk and at interfaces of PSCs (Ahmadi et al., 2017), and this result indicates that the FDC-2-5Cl could

suppress the trap states at perovskite/spiro-OMeTAD interface. The hysteresis characteristics of PSCs without and with FDC-2-5Cl treatment are shown in Figure 4F. The hysteresis index could be defined as HI = ($PCE_{reverse}$-$PCE_{forward}$)/$PCE_{reverse}$. The device with FDC-2-5Cl shows a lower hysteresis index of 2.45% than that of 13.54% for pristine device. The suppressed hysteresis behavior could be due to the reduced the surface defects of perovskite film with FDC-2-5Cl treatment.

To further investigate the charge recombination process and improved V_{oc} of PSCs with FDC-2-5Cl treatment, we studied the relationship between V_{oc} and light intensity, as shown in Figure 4G. Both PSCs without and with FDC-2-5Cl treatment show a linear relationship between V_{oc} and log scale of light intensity. It is noticed that the PSC with FDC-2-5Cl treatment shows a smaller slope of 1.38 kT/q than pristine PSCs (1.88 kT/q), where k is Boltzmann constant, T is temperature, and q is elementary charge. It is reported that the deviation of slope from kT/q reflects the trap-assisted recombination in devices (Yang et al., 2016). The lower slope of PSC with FDC-2-5Cl treatment indicates the reduced trap density and suppressed trap-assisted recombination. We further carried out the capacitance-voltage (C-V) measurement to study the V_{oc} improvement of PSCs with FDC-2-5Cl treatment. The built-in potential (V_{bi}) could be expressed according to the Mott-Schottky relationship. As shown in Figure 4H, the device with FDC-2-5Cl shows a V_{bi} of 0.94 V which is larger than that of pristine devices (0.90 V). The FDC-2-5Cl treatment exhibits the p-type doping effect and causes the surface energy band to bend upward. The upward energy band increases the V_{bi}. The improved V_{bi} is help to charge carrier separation. To further evaluate the charge transport dynamics in PSCs without and with FDC-2-5Cl treatment, we carried out the electrical impedance spectroscopy (EIS) measurement. The devices were measured in dark and with a bias voltage of 1 V. The Nyquist plots of devices are shown in Figure S12, the inset displays the circuit model, the arc at high frequency is related to the transfer resistance (R_{tr}) and the arc at low frequency is related to the recombination resistance (R_{rec}), and the series resistance (R_s) is caused by other layers except perovskite. Table S3 lists the fitting parameters of EIS spectra. The device with FDC-2-5Cl treatment shows a smaller R_{tr} of 2.70×10^4 Ω and larger R_{rec} 3.20×10^6 Ω than pristine device ($R_{tr} = 5.64 \times 10^4$ Ω and $R_{rec} = 1.08 \times 10^5$ Ω), which indicates the enhanced charger transfer and suppressed charge recombination in PSCs with FDC-2-5Cl treatment. This result is consistent with the previous results.

Finally, the long-term stability of devices without and with FDC-2-5Cl treatment was evaluated. Since the humidity seriously affects the stability of PSCs, we first measured the water contact angles of perovskite films without and with FDC-2-5Cl treatment. The perovskite film with FDC-2-5Cl treatment exhibits a larger contact angle (74.39°) than the pristine perovskite film (54.08°), as shown in the inset of Figure 4I. The increased contact angle is due to the hydrophobicity of FDC-2-5Cl caused by the aromatic side chains, and this result is also consistent with the decreased surface energy of perovskite with FDC-2-5Cl treatment from first-principles calculations. The increased water contact angle of perovskite film with FDC-2-5Cl treatment means the enhanced the humidity stability of perovskite film. The PSCs were stored in an oxygen-containing atmosphere in dark with a relative humidity of ≈60% and a temperature of 20–30°C to measure the long-term stability. The PSC with FDC-2-5Cl treatment shows the significantly enhanced stability (Figure 4I), and maintains 88% of its initial performance after 1008 hr exposure in air ambient condition. However, the pristine PSC only maintains 70% of its initial performance. The significantly improved stability is due to the enhanced hydrophobicity and improved film quality of perovskite film with FDC-2-5Cl treatment. We compared the effect of FDC-2-5Cl treatment on PSCs characteristics with other organic molecules reported in recent literatures, as shown in Table S4. The PSCs with FDC-2-5Cl treatment shows relatively high efficiency and long-term stability.

Conclusions

In conclusion, we have introduced an extended benzopentafulvalene compound with pentachlorophenyl group (FDC-2-5Cl) to passivate the perovskite film. It was found that FDC-2-5Cl could bond with perovskite film by Pb-Cl bond and hydrogen-bond, which could passivate the defects at surface and grain boundary of perovskite film and reduce the charge carrier recombination at perovskite/spiro-OMeTAD interface. Further first-principles calculations reveal that the FDC-2-5Cl treatment increases defect formation energy and reduces surface energy of perovskite. Meanwhile, the FDC-2-5Cl could accept the electrons from perovskite as a p-type dopant, and induced the band bending at perovskite surface, which enhances the charge transfer at perovskite/spiro-OMeTAD interface. Further, the FDC-2-5Cl treatment layer also improves the hydrophobicity of perovskite film, leading to an improved humidity stability of PSCs. As a result, the PSC with FDC-2-5Cl treatment reaches a high PCE of 21.16% (20.7% of stabilized efficiency) with a high V_{oc} of 1.14 V. The device with FDC-2-5Cl treatment also exhibits remarkable long-term stability, retaining

88% of its initial performance after 1008 hr storage in high humidity condition. This result helps to provide a useful strategy to fabricate the high efficient and stable PSCs.

Limitations of the study

In this work, we introduced FDC-2-5Cl to treat the perovskite surface. The FDC-2-5Cl with pentachlorophenyl group could accept the electrons from perovskite as a p-type dopant and passivate the undercoordinated Pb^{2+} ions and iodine defects with Pb-Cl and hydrogen bond interactions. The device with FDC-2-5Cl treatment shows outstanding PCE with great long-term stability. It would be more interesting to study the depth of p-doping effect of FDC-2-5Cl.

Resource availability

Lead contact

Further information and requests for resources should be directed to and will be fulfilled by the lead contact, Jingjing Chang (jjingchang@xidian.edu.cn).

Materials availability

All chemicals were obtained from commercial resources and used as received.

Data and code availability

This study did not generate any datasets.

METHODS

All methods can be found in the accompanying transparent methods supplemental file.

SUPPLEMENTAL INFORMATION

Supplemental information can be found online at https://doi.org/10.1016/j.isci.2021.102276.

AUTHOR CONTRIBUTIONS

X.G. conducted the experiment. J.J.C. conceived the idea. X.W. and Z.B.Z. provided material support. J.S. contributed to the first-principles calculations. Q.R.W. contributed to some characterizations of perovskite films. J.J.C., J.C.Z., and Y.H. supervised the project. X.G., J.S., Z.H.L., and J.J.C. wrote the paper.

DECLARATION OF INTERESTS

The authors declare no conflicts of interest.

REFERENCES

Ahmadi, M., Wu, T., and Hu, B. (2017). A review on organic-inorganic halide perovskite photodetectors: device engineering and fundamental physics. Adv. Mater. 29, 1605242.

Aristidou, N., Eames, C., Sanchez-Molina, I., Bu, X., Kosco, J., Islam, M.S., and Haque, S.A. (2017). Fast oxygen diffusion and iodide defects mediate oxygen-induced degradation of perovskite solar cells. Nat. Commun. 8, 15218.

Ball, J.M., and Petrozza, A. (2016). Defects in perovskite-halides and their effects in solar cells. Nat. Energy 1, 16149.

Berhe, T.A., Su, W.-N., Chen, C.-H., Pan, C.-J., Cheng, J.-H., Chen, H.-M., Tsai, M.-C., Chen, L.-Y.,

Dubale, A.A., and Hwang, B.-J. (2016). Organometal halide perovskite solar cells: degradation and stability. Energy Environ. Sci. 9, 323–356.

Biswas, K., Rathore, E., Maji, K., Rao, D., and Saha, B. (2020). Charge transfer in the heterostructure of $CsPbBr_3$ nanocrystals with nitrogen-doped carbon dots. J. Phys. Chem. Lett. 11, 8002–8007.

Chen, P., Bai, Y., Wang, S., Lyu, M., Yun, J.-H., and Wang, L. (2018). In situ growth of 2D perovskite capping layer for stable and efficient perovskite solar cells. Adv. Funct. Mater. 28, 1706923.

Eames, C., Frost, J.M., Barnes, P.R.F., O'Regan, B.C., Walsh, A., and Islam, M.S. (2015). Ionic transport in hybrid lead iodide perovskite solar cells. Nat. Commun. 6, 7497.

Guo, X., Lin, Z., Ma, J., Hu, Z., Su, J., Zhang, C., Zhang, J., Chang, J., and Hao, Y. (2019). Low temperature combustion synthesized indium oxide electron transport layer for high performance and stable perovskite solar cells. J. Power Sources 438, 226981.

Guo, X., Zhang, B., Lin, Z., Ma, J., Su, J., Zhu, W., Zhang, C., Zhang, J., Chang, J., and Hao, Y. (2018a). Interface engineering of TiO$_2$/perovskite interface via fullerene derivatives for high performance planar perovskite solar cells. Org. Electron. 62, 459–467.

Guo, X., Zhang, B., Lin, Z., Su, J., Yang, Z., Zhang, C., Chang, J., Liu, S. (Frank), and Hao, Y. (2018b). Highly efficient perovskite solar cells based on a dopant-free conjugated DPP polymer hole transport layer: influence of solvent vapor annealing. Sustain. Energy Fuels 2, 2154–2159.

Jiang, Q., Ni, Z., Xu, G., Lin, Y., Rudd, P.N., Xue, R., Li, Y., Li, Y., Gao, Y., and Huang, J. (2020). Interfacial molecular doping of metal halide perovskites for highly efficient solar cells. Adv. Mater. 32, 2001581.

Jiang, Q., Zhao, Y., Zhang, X., Yang, X., Chen, Y., Chu, Z., Ye, Q., Li, X., Yin, Z., and You, J. (2019). Surface passivation of perovskite film for efficient solar cells. Nat. Photon. 13, 460–466.

Kojima, A., Teshima, K., Shirai, Y., and Miyasaka, T. (2009). Organometal halide perovskites as visible-light sensitizers for photovoltaic cells. J. Am. Chem. Soc. 131, 6050–6051.

Li, H., Shi, J., Deng, J., Chen, Z., Li, Y., Zhao, W., Wu, J., Wu, H., Luo, Y., Li, D., and Meng, Q. (2020). Intermolecular π–π conjugation self-assembly to stabilize surface passivation of highly efficient perovskite solar cells. Adv. Mater. 32, 1907396.

Li, N., Tao, S., Chen, Y., Niu, X., Onwudinanti, C.K., Hu, C., Qiu, Z., Xu, Z., Zheng, G., Wang, L., et al. (2019). Cation and anion immobilization through chemical bonding enhancement with fluorides for stable halide perovskite solar cells. Nat. Energy 4, 408–415.

Lin, Q., Armin, A., Nagiri, R.C.R., Burn, P.L., and Meredith, P. (2015). Electro-optics of perovskite solar cells. Nat. Photon. 9, 106–112.

Liu, Z., Chang, J., Lin, Z., Zhou, L., Yang, Z., Chen, D., Zhang, C., Liu, S.F., and Hao, Y. (2018). High-performance planar perovskite solar cells using low temperature, solution-combustion-based nickel oxide hole transporting layer with efficiency exceeding 20%. Adv. Energy Mater. 8, 1703432.

Lv, Y., Shi, Y., Song, X., Liu, J., Wang, M., Wang, S., Feng, Y., Jin, S., and Hao, C. (2018). Bromine doping as an efficient strategy to reduce the interfacial defects in hybrid two-dimensional/ three-dimensional stacking perovskite solar cells. ACS Appl. Mater. Inter. 10, 31755–31764.

Meng, L., Sun, C., Wang, R., Huang, W., Zhao, Z., Sun, P., Huang, T., Xue, J., Lee, J.-W., Zhu, C., et al. (2018). Tailored phase conversion under conjugated polymer enables thermally stable perovskite solar cells with efficiency exceeding 21%. J. Am. Chem. Soc. 140, 17255–17262.

Muduli, S., Pandey, P., Devatha, G., Babar, R., M T, Kothari, D.C., Kabir, M., Pillai, P.P., and Ogale, S. (2018). Photoluminescence quenching in self-assembled CsPbBr$_3$ quantum dots on few-layer black phosphorus sheets. Angew. Chem. Int. Ed. 57, 7682–7686.

Noel, N.K., Habisreutinger, S.N., Pellaroque, A., Pulvirenti, F., Wenger, B., Zhang, F., Lin, Y.-H., Reid, O.G., Leisen, J., Zhang, Y., et al. (2019). Interfacial charge-transfer doping of metal halide perovskites for high performance photovoltaics. Energy Environ. Sci. 12, 3063–3073.

Noh, J.H., Im, S.H., Heo, J.H., Mandal, T.N., and Seok, S.I. (2013). Chemical management for colorful, efficient, and stable inorganic–organic hybrid nanostructured solar cells. Nano Lett. 13, 1764–1769.

NREL Chart. (2020). Best research-cell efficiencies. https://www.nrel.gov/pv/assets/ pdfs/best-research-cell-efficiencies.20200925. pdf

Qian, F., Yuan, S., Cai, Y., Han, Y., Zhao, H., Sun, J., Liu, Z., and Liu, S. (Frank) (2019). Novel surface passivation for stable FA$_{0.85}$MA$_{0.15}$PbI$_3$ perovskite solar cells with 21.6% efficiency. Sol. RRL 3, 1900072.

Saidaminov, M.I., Abdelhady, A.L., Murali, B., Alarousu, E., Burlakov, V.M., Peng, W., Dursun, I., Wang, L., He, Y., Maculan, G., et al. (2015). High-quality bulk hybrid perovskite single crystals within minutes by inverse temperature crystallization. Nat. Commun. 6, 7586.

Saidaminov, M.I., Kim, J., Jain, A., Quintero-Bermudez, R., Tan, H., Long, G., Tan, F., Johnston, A., Zhao, Y., Voznyy, O., and Sargent, E.H. (2018). Suppression of atomic vacancies via incorporation of isovalent small ions to increase the stability of halide perovskite solar cells in ambient air. Nat. Energy 3, 648–654.

Seo, H., Kim, H., Lee, J., Park, M., Jeong, S., Kim, Y., Kwon, S., Han, T., Yoo, S., and Lee, T. (2017). Efficient flexible organic/inorganic hybrid perovskite light-emitting diodes based on graphene anode. Adv. Mater. 29, 1605587.

Shao, Y., Xiao, Z., Bi, C., Yuan, Y., and Huang, J. (2014). Origin and elimination of photocurrent hysteresis by fullerene passivation in CH$_3$NH$_3$PbI$_3$ planar heterojunction solar cells. Nat. Commun. 5, 5784.

Sherkar, T.S., Momblona, C., Gil-Escrig, L., Ávila, J., Sessolo, M., Bolink, H.J., and Koster, L.J.A. (2017). Recombination in perovskite solar cells: significance of grain boundaries, interface traps, and defect ions. ACS Energy Lett 2, 1214–1222.

Shi, D., Adinolfi, V., Comin, R., Yuan, M., Alarousu, E., Buin, A., Chen, Y., Hoogland, S., Rothenberger, A., Katsiev, K., et al. (2015). Low trap-state density and long carrier diffusion in organolead trihalide perovskite single crystals. Science 347, 519–522.

Son, D.-Y., Kim, S.-G., Seo, J.-Y., Lee, S.-H., Shin, H., Lee, D., and Park, N.-G. (2018). Universal

approach toward hysteresis-free perovskite solar cell via defect engineering. J. Am. Chem. Soc. 140, 1358–1364.

Stranks, S.D., Eperon, G.E., Grancini, G., Menelaou, C., Alcocer, M.J.P., Leijtens, T., Herz, L.M., Petrozza, A., and Snaith, H.J. (2013). Electron-hole diffusion lengths exceeding 1 micrometer in an organometal trihalide perovskite absorber. Science 342, 341–344.

Stranks, S.D., and Snaith, H.J. (2015). Metal-halide perovskites for photovoltaic and light-emitting devices. Nat. Nanotechnol. 10, 391–402.

Sun, Q., Fassl, P., Becker-Koch, D., Bausch, A., Rivkin, B., Bai, S., Hopkinson, P.E., Snaith, H.J., and Vaynzof, Y. (2017). Role of microstructure in oxygen induced photodegradation of methylammonium lead triiodide perovskite films. Adv. Energy Mater. 7, 1700977.

Tavakoli, M.M., Yadav, P., Prochowicz, D., Sponseller, M., Osherov, A., Bulović, V., and Kong, J. (2019). Controllable perovskite crystallization via antisolvent technique using chloride additives for highly efficient planar perovskite solar cells. Adv. Energy Mater. 9, 1803587.

Turren-Cruz, S.-H., Saliba, M., Mayer, M.T., Juárez-Santiesteban, H., Mathew, X., Nienhaus, L., Tress, W., Erodici, M.P., Sher, M.-J., Bawendi, M.G., et al. (2018). Enhanced charge carrier mobility and lifetime suppress hysteresis and improve efficiency in planar perovskite solar cells. Energy Environ. Sci. 11, 78–86.

Wang, S., Jiang, Y., Juarez-Perez, E.J., Ono, L.K., and Qi, Y. (2016). Accelerated degradation of methylammonium lead iodide perovskites induced by exposure to iodine vapour. Nat. Energy 2, 16195.

Wang, X., Zhang, Z., Guo, J., Liu, C., Hu, Y., Xiao, H., Xie, S., Wu, J., and Zeng, Z. (2020). Ring-expansion approach towards extended asymmetric benzopentafulvalenes: overcrowded olefinic structure and chain length-dependent properties. Org. Chem. Front. 7, 2247–2254.

Wehrenfennig, C., Eperon, G.E., Johnston, M.B., Snaith, H.J., and Herz, L.M. (2014). High charge carrier mobilities and lifetimes in organolead trihalide perovskites. Adv. Mater. 26, 1584–1589.

Wolff, C.M., Canil, L., Rehermann, C., Ngoc Linh, N., Zu, F., Ralaiarisoa, M., Caprioglio, P., Fiedler, L., Stolterfoht, M., Kogikoski, S., et al. (2020). Perfluorinated self-assembled monolayers enhance the stability and efficiency of inverted perovskite solar cells. ACS Nano 14, 1445–1456.

Xi, H., Tang, S., Ma, X., Chang, J., Chen, D., Lin, Z., Zhong, P., Wang, H., and Zhang, C. (2017). Performance enhancement of planar heterojunction perovskite solar cells through tuning the doping properties of hole-transporting materials. ACS Omega 2, 326–336.

Xiao, Z., Dong, Q., Bi, C., Shao, Y., Yuan, Y., and Huang, J. (2014). Solvent annealing of perovskite-induced crystal growth for photovoltaic-device efficiency enhancement. Adv. Mater. 26, 6503–6509.

Yang, D., Zhou, X., Yang, R., Yang, Z., Yu, W., Wang, X., Li, C., Liu, S. (Frank), and Chang,

R.P.H. (2016). Surface optimization to eliminate hysteresis for record efficiency planar perovskite solar cells. Energy Environ. Sci. *9*, 3071–3078.

Yang, Y., Feng, S., Li, M., Li, F., Zhang, C., Han, Y., Li, L., Yuan, J., Cao, L., Wang, Z., et al. (2018). Enormously improved $CH_3NH_3PbI_3$ film surface for environmentally stable planar perovskite solar cells with PCE exceeding 19.9%. Nano Energy *48*, 10–19.

Yue, M., Su, J., Zhao, P., Lin, Z., Zhang, J., Chang, J., and Hao, Y. (2019). Optimizing the performance of $CsPbI_3$-based perovskite solar cells via doping a ZnO electron transport layer coupled with interface engineering. Nano-Micro Lett. *11*, 91.

Zhang, B., Su, J., Guo, X., Zhou, L., Lin, Z., Feng, L., Zhang, J., Chang, J., and Hao, Y. (2020). NiO/ Perovskite heterojunction contact engineering for highly efficient and stable perovskite solar cells. Adv. Sci. *7*, 1903044.

Zhao, H., Wang, S., Sun, M., Zhang, F., Li, X., and Xiao, Y. (2018). Enhanced stability and optoelectronic properties of $MAPbI_3$ films by a cationic surface-active agent for perovskite solar cells. J. Mater. Chem. A 6, 10825–10834.

Zhou, L., Guo, X., Lin, Z., Ma, J., Su, J., Hu, Z., Zhang, C., Liu, S. (Frank), Chang, J., and Hao, Y. (2019a). Interface engineering of low temperature processed all-inorganic $CsPbI_2Br$ perovskite solar cells toward PCE exceeding 14%. Nano Energy *60*, 583–590.

Zhou, L., Lin, Z., Ning, Z., Li, T., Guo, X., Ma, J., Su, J., Zhang, C., Zhang, J., Liu, S., et al. (2019b). Highly efficient and stable planar perovskite solar cells with modulated diffusion passivation toward high power conversion efficiency and ultrahigh fill factor. Sol. RRL *3*, 1900293.

Zhu, H., Fu, Y., Meng, F., Wu, X., Gong, Z., Ding, Q., Gustafsson, M.V., Trinh, M.T., Jin, S., and Zhu, X. (2015). Lead halide perovskite nanowire lasers with low lasing thresholds and high quality factors. Nat. Mater. *14*, 636–642.

Zou, Y., Wang, H.-Y., Qin, Y., Mu, C., Li, Q., Xu, D., and Zhang, J.-P. (2019). Reduced defects of $MAPbI_3$ thin films treated by FAI for high-performance planar perovskite solar cells. Adv. Funct. Mater. *29*, 1805810.

Supplemental information

Synergetic surface charge transfer

doping and passivation toward high

efficient and stable perovskite solar cells

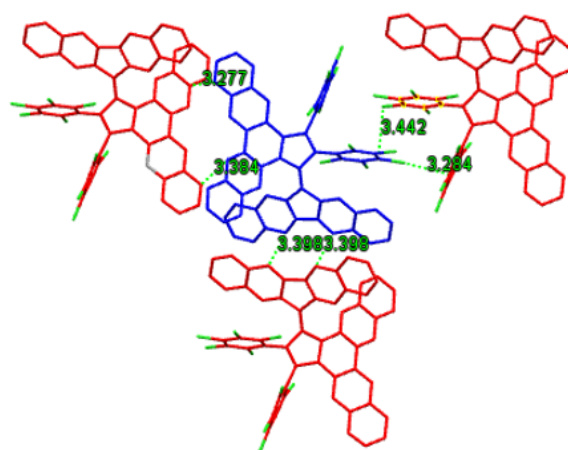Xing Guo, Jie Su, Zhenhua Lin, Xinhao Wang, Qingrui Wang, Zebing Zeng, Jingjing Chang, and Yue Hao

Figure S1. The crystal packing of FDC-2-5Cl, and green represents chlorine. The typical intermolecular distance and molecular interactions between different part. Related to Figure 1.
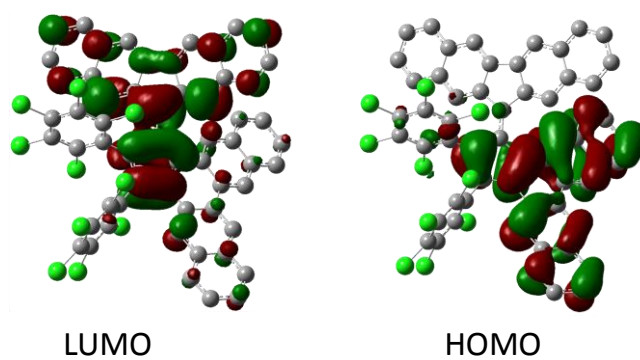

LUMO   HOMO

Figure S2. Calculated molecular orbital profiles of the HOMO and LUMO of FDC-2-5Cl. Related to Figure 1.
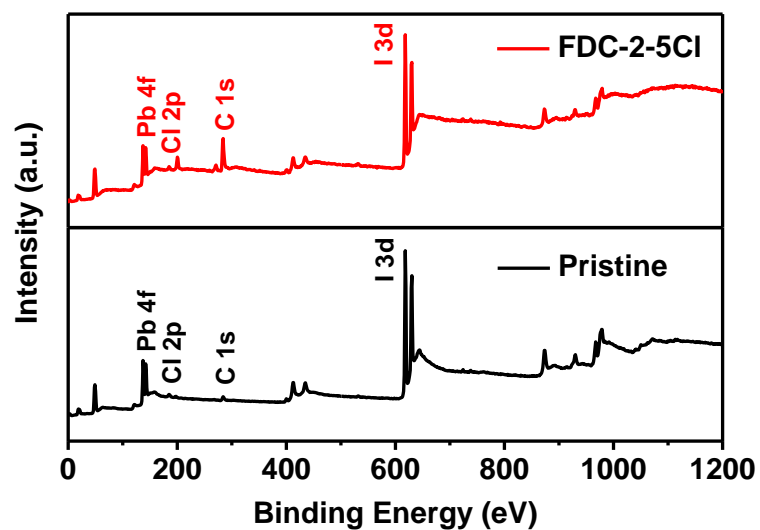
Figure S3. The full XPS spectra of perovskite films without and with FDC-2-5Cl treatment.
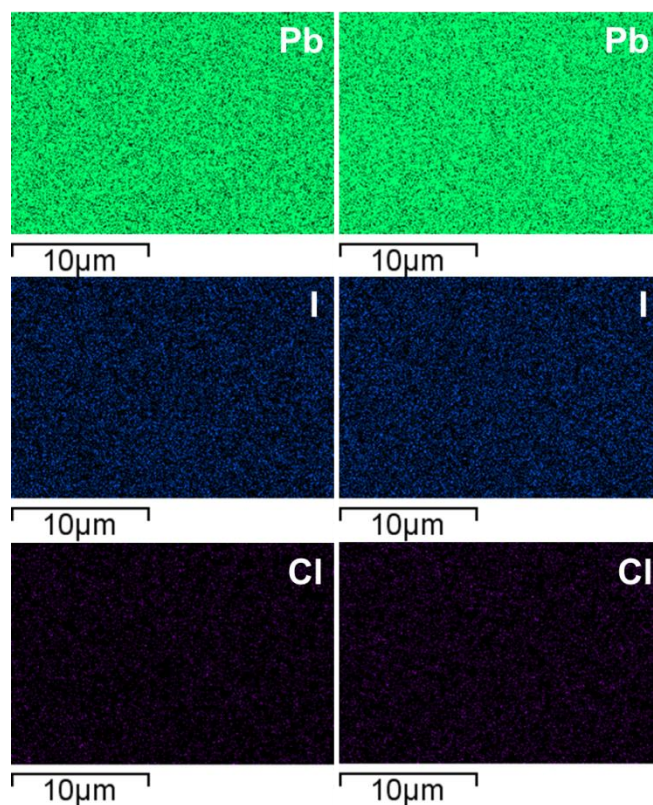
Related to Figure 1.

Figure S4. The SEM-EDS mapping images of perovskite films without (left) and with (right)
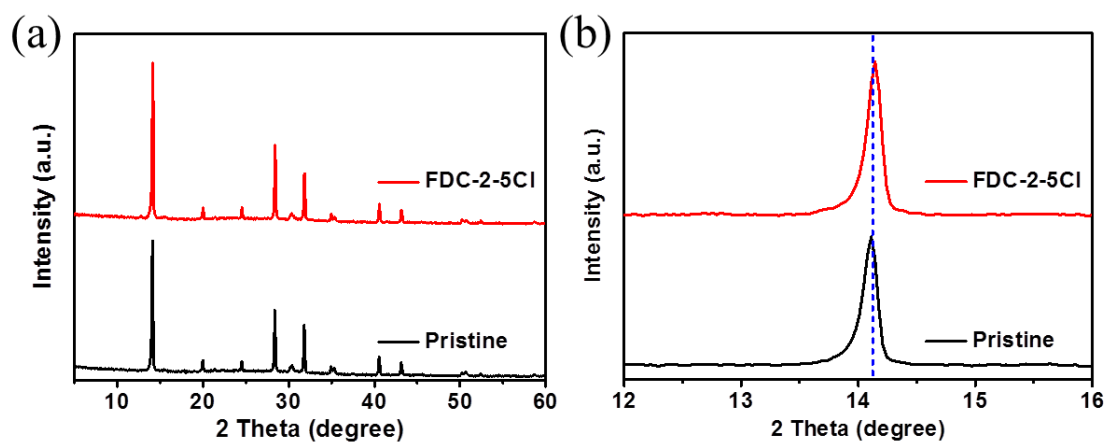
FDC-2-5Cl treatment. Related to Figure 1.

Figure S5. (a) XRD patterns of perovskite films without and with FDC-2-5Cl treatment. **(b)** Zoom-in image of (110) peak of Figure a. Related to Figure 1.
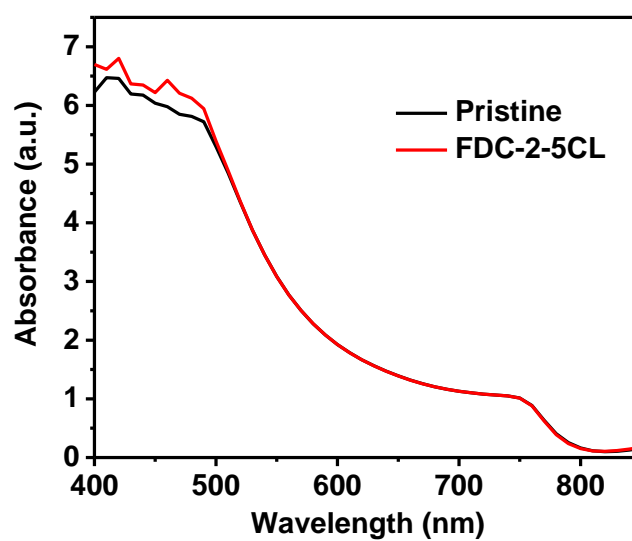

Figure S6. UV-vis absorption spectra of perovskite films without and with FDC-2-5Cl treatment. Related to Figure 2.
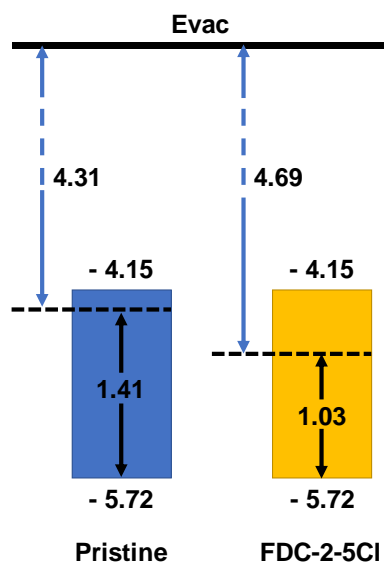
Figure S7. Energy level schemes of perovskite film without and with FDC-2-5Cl treatment derived from UPS spectra. Related to Figure 2.
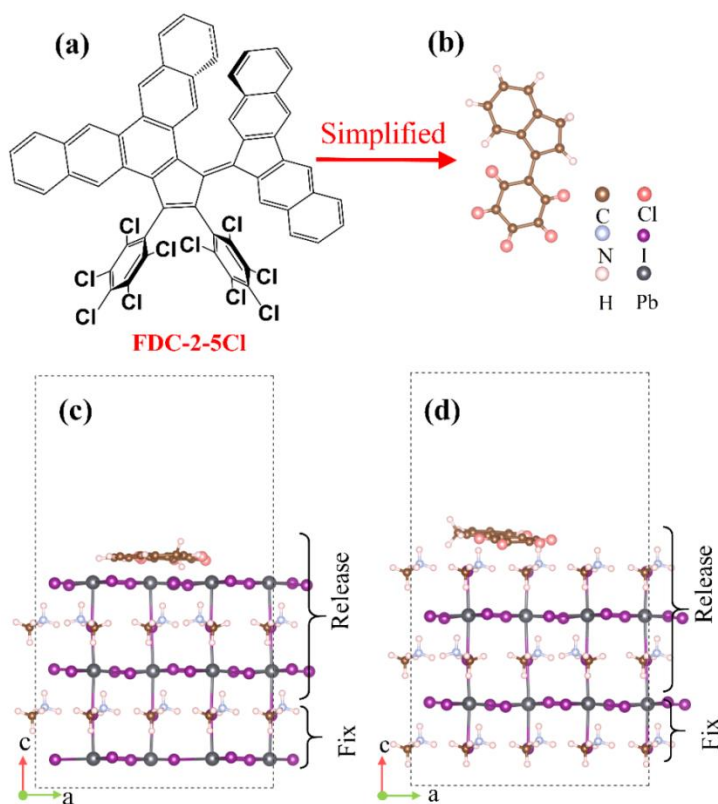

Figure S8. Side views of (a) FDC-2-5Cl and (b) simplified FDC-2-5Cl. (c) Simplified FDC-2-5Cl treated MAPbI$_3$ (001) surface with with V_I and (d) simplified FDC-2-5Cl treated MAPbI$_3$ (001) with I_{Pb}. Related to Figure 3.
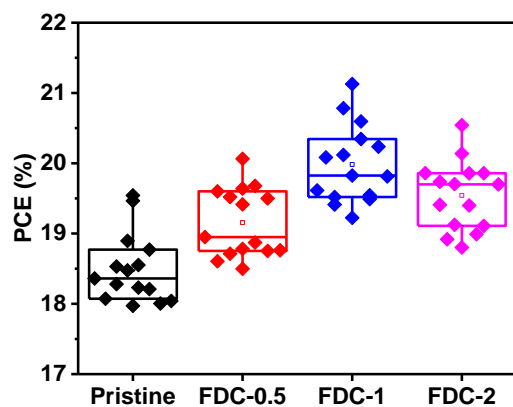
Figure S9. PCE distribution of PSCs with different concentrations FDC-2-5Cl treatment, 0.5 mg/mL (FDC-0.5), 1 mg/mL (FDC-1), and 2 mg/mL (FDC-2). Related to Figure 4.
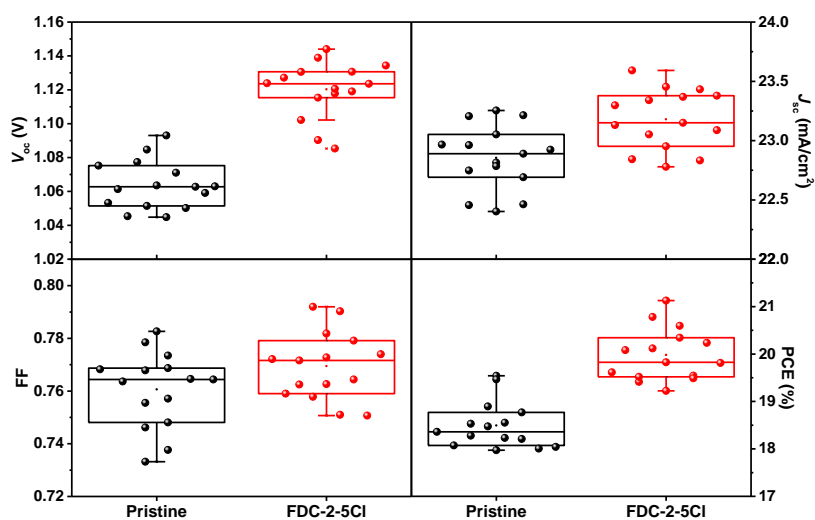

Figure S10. Device performance distribution of PSCs without and with FDC-2-5Cl treatment. Related to Figure 4.
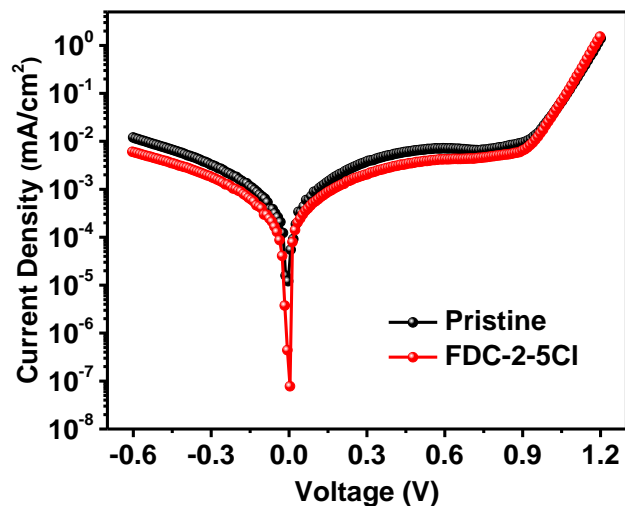
Figure S11. The dark *J* - *V* characteristics of PSCs without and with FDC-2-5Cl treatment. Related to Figure 4.

Figure S12. EIS spectra of PSCs without and with FDC-2-5Cl treatment. Related to Figure 4.

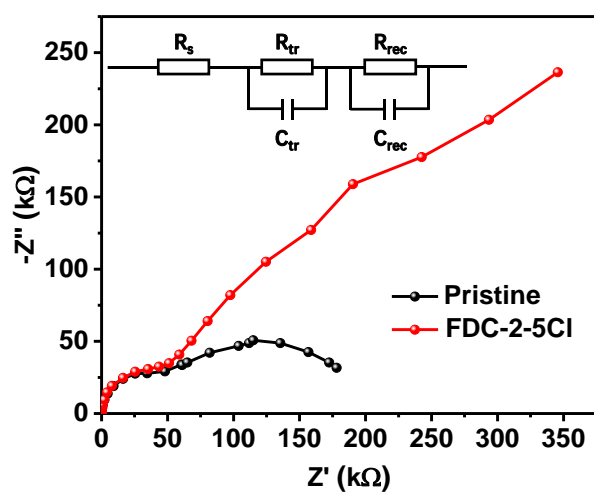**Table S1.** The electrical characters of FDC-2-5Cl. Related to Figure 1.

Compound	HOMO (eV)	LUMO (eV)	μ_e $cm^2V^{-1}s^{-1}$	μ_h $cm^2V^{-1}s^{-1}$
FDC-2-5Cl	-5.45	-3.91	2.57×10^{-4}	1.06×10^{-4}

Table S2. Fitting parameters of TRPL curves. Related to Figure 4.

Samples	τ_1 (ns)	A_1	τ_2 (ns)	A_2	τ_{ave} (ns)
Perovskite	24.60	0.28	101.25	0.72	94.60
Perovskite (FDC-2-5Cl)	15.11	0.46	82.76	0.54	73.52
Perovskite/Spiro-OMeTAD	4.00	0.99	88.63	0.01	23.53
Perovskite (FDC-2-5Cl)/Spiro-OMeTAD	3.61	0.99	62.08	0.01	9.92

Table S3. Fitting parameters of EIS spectra. Related to Figure S12.

Samples	R_s (Ω)	R_{tr} (Ω)	C_{tr} (F)	R_{rec} (Ω)	C_{rec} (F)
Pristine	25.44	5.64×10^4	6.80×10^{-9}	1.08×10^5	1.25×10^{-7}
FDC-2-5Cl	22.50	2.70×10^4	6.87×10^{-9}	3.20×10^6	1.70×10^{-7}

Table S4. The comparison of device characteristics passivated by the organic molecule in our work and related literatures. Related to Figure 4.

Passivation molecule	PCE	V_{oc}	Hysteresis index	Long-term stability	References
FDC-2-5Cl	21.16 %	1.14 V	2.45 %	88 %, 1008h, in air, 60% RH, 20-30 ^{o}C	This work
TBAPF$_6$	21.23 %	1.103 V	0.4 %	90 %, 400 h, in air, 45% RH, room temperature	(Xiong et al., 2021)
ML	21.4 %	1.16 V	3.74 %	70.6 %, 96 h, 70% RH	(Wu et al., 2020)
F5PEA	21.10 %	1.196 V	0.57 %	83 %, 720 h, 45-60% RH	(Ye et al., 2020)

TCPBr	20.13 %	1.14 V	5.4 %	90.7 %, 1000 h, 60-80 %RH, room temperature	(He et al., 2020)
TPFP	21.04 %	1.16 V		63 %, 336 h, 75% RH	(Yang et al., 2020)
TBPO	22.1 %	1.14 V	5.88 %	90%, 3500 h, in dark and ambient condition	(Li et al., 2020)

Transparent Methods

Materials: All materials Tin (IV) oxide (SnO$_2$, 15 % in H$_2$O colloidal dispersion, Alfa Aesar), lead iodide (II) (PbI$_2$, 99.999 %, Alfa), lead (II) chloride (PbCl$_2$, 99.999 %, Alfa), cesium iodide (CsI, 99.998 %, Alfa), Methylammonium iodide (MAI, 99.8 %, Dyesol), Formamidinium iodide (FAI, 99.8 %, Dyesol) and spiro-OMeTAD (Xi'an Polymer Light Technology Corp.) are purchased without further purification. All solvent, N,N-Di-methylformamide (DMF, 99.8 %), isopropanol (IPA, 99.5 %) and chlorobenzene (CB, 99.5 %) are purchased from Sigma-Aldrich.

Device Fabrication: The indium tin oxide (ITO) glass substrates (around 2×2.5 cm^2 in size, 10 Ω per square) were cleaned sequentially with detergent, deionized water, acetone, and ethanol in an ultrasonic wave for 20 min, respectively. The SnO$_2$ (15 % in H$_2$O colloidal dispersion) solution was diluted to 5 % and spin coated on the ITO substrates at 4000 rpm for 40 s and annealed at 150 °C for 30 min on a hot plate to form SnO$_2$ layer. After cooling down to room temperature, the substrates were transfered into a nitrogen-filled glove box. For the perovskite film fabrication, 1.36 M PbI$_2$, 0.24 M PbCl$_2$ and 0.08 M CsI were dissolved in the DMF and stirred for 3 h at 70 °C. 70 mg MAI and 30 mg FAI were dissolved in 1 mL IPA with 10 μL DMF added. After that, around 70 μL PbX$_2$ precursor solution was spin coated onto SnO$_2$ substrates at 3000 rpm for 45 s. Then, 200 μL MAI:FAI solution was spin coated onto the PbX$_2$ at 3000 rpm for 45 s. Then the samples were thermally annealed on a hot plate at 100 °C for 10 min. For the FDC-2-5Cl treatment, the FDC-2-5Cl was dissolved in CB at different concentration and spin-coated on the perovskite film and annealed 100 °C for 3 mins. The spiro-OMeTAD was spin-coated on the top of the perovskite layer at 4000 rpm for 45 s. The spiro-OMeTAD solution was prepared by dissolved 72.5 mg spiro-OMeTAD in 1 mL chlorobenzene and added 17.5 μL Li-TFSI solution (520 mg/mL in acetonitrile), 28.8 μL FK209 solution (300 mg/mL in acetonitrile) and 28.8 μL 4-tertbutylpyridine (tBP). Finally, 100 nm Ag was thermally evaporated on the top of spiro-OMeTAD as the electrodes. The area of the device was 7.5 mm^2 defined by the metal mask. For the electron-only device (glass/ITO/SnO$_2$/perovskite(FDC-2-5Cl)/PCBM/Ag) and hole-only device (glass/ITO/NiO/perovskite(FDC-2-5Cl)/spiro-OMeTAD/Ag), the fabrication methods of SnO$_2$, perovskite, FDC-2-5Cl, spiro-OMeTAD and Ag are same with the method used in PSCs fabrication. The NiO layer was fabricated by a combustion method. The NiO precursor was prepared by dissolving 270.79 mg Ni(NO$_3$)$_2$·6H$_2$O in 2-methoxyethanol (10 mL). After the solution was stirred at 50 °C for 1 h, 100 μL

acetylacetone was added to the solution, and then the solution was further stirred overnight at room temperature. The NiO layer was fabricated by spin-coating the precursor solution on ITO substrates at 3000 rpm for 45 s and annealed at 250 °C for 45 min. The PCBM layer was fabricated by spin-coating the PCBM solution (20 mg/mL in chlorobenzene) on the top of the perovskite layer at 2000 rpm for 40 s.

Characterization: The current density - voltage (*J - V*) characteristics of PSCs were measured under AM 1.5 G irradiation (100 mW cm^{-2}) by using a Keithley 2400 source meter, and the solar simulator (XES-70S1) was calibrated against an NREL certified silicon reference solar cell. The IPCE was measured by a solar cell quantum efficiency measuring system (SCS10-X150, Zolix instruments. Co. Ltd.). All the tests were carried out in ambient air in a temperature of 28 - 35 °C and a relative humidity of approximately 30 - 80 %. The *C - V* and EIS were measured by an electrochemical workstation (DH7001). The morphology of the perovskite layer was measured by SEM (JSM-7800F). XRD test was conducted on Bruker D8 Advance XRD. PL and TR-PL were measured using the Pico Quant Fluotime 300 by using a 510 nm picosecond pulsed laser. The UV-vis absorption spectra were recorded using an ultraviolet-visible spectrophotometer (Perkin-Elmer Lambda 950). The water contact angle measurement was carried out by a contact angle meter (JC2000DM, Beijing Zhongyikexin Science and Technology Co. Ltd., Beijing, China). XPS measurements were performed by the Escalab 250Xi with a source of monochromatic Al-Ka (1486.6 eV). The UPS measurements were carried out using a He I (*hv* = 21.22 eV) source.

DFT calculation: All calculations were based on density functional theory (DFT)(Hohenberg and Kohn, 1964) as implemented in the Vienna ab initio simulation package (VASP)(Kresse and Furthmüller, 1996a, 1996b) code with projector augmented wave (PAW) method.(Blochl, 1994; Kohn and Sham, 1965; Kresse and Joubert, 1999) The Perdew-Burke-Ernzerhof (PBE) functional within the generalized gradient approximation (GGA) was employed to describe the exchange-correlation interaction.(Perdew et al., 1996) The van der Waals interaction is considered using DFT-D2 method. The plane-wave cut-off energy of 400 eV and Monkhorst-Pack k-point meshes spanning less than 0.02 Å^{-3} in the Brillouin zone were chosen. All structures were relaxed until the residual force on each atom less than 0.01 eV/Å. The self-consistent convergence accuracy was set at 10^{-5} eV/atom in the structural calculation. The MAI and PbI terminated defective MAPbI$_3$ surfaces were modelled employing periodically repeated slabs using the (2 × 2) supercell with adsorbates on one side, as shown in Figure S8. The slabs were seven layers thick, and the bottom three layers were kept fixed in their bulk positions during relaxations. A vacuum region more than 15 Å in the z-direction in conjunction with the dipole correction to avoid the fictitious interaction with its periodic images. According to previous reports, the large FDC-2-5Cl molecular was separated into two parts to successfully obtain the effect of FDC-2-5Cl, as demonstrated in Figure S8.

Supplemental References

Blochl, P.E., 1994. Projector augmented-wave method. Phys. Rev. B 50, 17953–17979.

Hohenberg, P., Kohn, W., 1964. Inhomogeneous Electron Gas. Phys. Rev. 136, B864–B871.

Kohn, W., Sham, L.J., 1965. Self-Consistent Equations Including Exchange and Correlation Effects. Phys. Rev. 140, A1133–A1138.

Kresse, G., Furthmüller, J., 1996a. Efficiency of ab-initio total energy calculations for metals and semiconductors using a plane-wave basis set. Comput. Mater. Sci. 6, 15–50.

Kresse, G., Furthmüller, J., 1996b. Efficient iterative schemes for ab initio total-energy calculations using a plane-wave basis set. Phys. Rev. B 54, 11169–11186.

Kresse, G., Joubert, D., 1999. From ultrasoft pseudopotentials to the projector augmented-wave method. Phys. Rev. B 59, 1758–1775.

Perdew, J.P., Burke, K., Ernzerhof, M., 1996. Generalized Gradient Approximation Made Simple. Phys. Rev. Lett. 77, 3865–3868.

He, Q., Worku, M., Xu, L., Zhou, C., Lteif, S., Schlenoff, J.B., Ma, B., 2020. Surface passivation of perovskite thin films by phosphonium halides for efficient and stable solar cells. J. Mater. Chem. A 8, 2039–2046.

Li, H., Shi, J., Deng, J., Chen, Z., Li, Y., Zhao, W., Wu, J., Wu, H., Luo, Y., Li, D., Meng, Q., 2020. Intermolecular π–π Conjugation Self‐Assembly to Stabilize Surface Passivation of Highly Efficient Perovskite Solar Cells. Adv. Mater. 32, 1907396.

Wu, Z., Jiang, M., Liu, Z., Jamshaid, A., Ono, L.K., Qi, Y., 2020. Highly Efficient Perovskite Solar Cells Enabled by Multiple Ligand Passivation. Adv. Energy Mater. 10, 1903696.

Xiong, S., Dai, Y., Yang, J., Xiao, W., Li, D., Liu, X., Ding, L., Gao, P., Fahlman, M., Bao, Q., 2021. Surface charge-transfer doping for highly efficient perovskite solar cells. Nano Energy 79, 105505.

Yang, Z., Dou, J., Kou, S., Dang, J., Ji, Y., Yang, G., Wu, W.Q., Kuang, D. Bin, Wang, M., 2020. Multifunctional Phosphorus-Containing Lewis Acid and Base Passivation Enabling Efficient and Moisture-Stable Perovskite Solar Cells. Adv. Funct. Mater. 30, 1910710.

Ye, J.Y., Tong, J., Hu, J., Xiao, C., Lu, H., Dunfield, S.P., Kim, D.H., Chen, X., Larson, B.W., Hao, J., Wang, K., Zhao, Q., Chen, Z., Hu, H., You, W., Berry, J.J., Zhang, F., Zhu, K., 2020. Enhancing Charge Transport of 2D Perovskite Passivation Agent for Wide-Bandgap Perovskite Solar Cells Beyond 21%. Sol. RRL 4, 2000082.